Geophysical Research Letters

RESEARCH LETTER
10.1029/2025GL115125

Driving Earth's Outer Radiation Belt With Alfvénic Turbulence

C. C. Chaston[1]

[1]Space Sciences Laboratory, University of California, Berkeley, Berkeley, CA, USA

Key Points:

- The global evolution of outer radiation belt electron distributions in observed Alfvénic turbulence is simulated
- Alfvénic turbulence drives radial transport and rapid relativistic electron loss to near-Earth space and the atmosphere
- Alfvénic turbulence drives the formation of "butterfly" electron pitch-angle distributions with exponential energy spectra

Supporting Information:

Supporting Information may be found in the online version of this article.

Correspondence to:

C. C. Chaston,
ccc@ssl.berkeley.edu

Citation:

Chaston, C. C. (2025). Driving Earth's outer radiation belt with Alfvénic turbulence. *Geophysical Research Letters*, *52*, e2025GL115125. https://doi.org/10.1029/2025GL115125

Received 27 JAN 2025
Accepted 11 APR 2025

Abstract Semi-empirical coefficients for electron transport in Alfvénic turbulence are used to drive the global evolution of energetic electron distributions through Earth's outer radiation belt. It is shown how these turbulent fields facilitate radial transport and pitch-angle scattering that drive losses through the magnetopause, into the plasma sheet, through the plasmapause and to the atmosphere. Butterfly distributions are formed due to pitch-angle scattering and the combined effect of the loss processes. For the observed spectrum of oscillations, it is estimated that Alfvénic turbulence drives order of magnitude depletions of outer radiation belt electron fluxes at relativistic energies over a period of a few hours. On the other hand, at lower energies, energization in transverse Alfvénic electric fields leads to enhancements of the electron spectrum to provide a source population for subsequent acceleration to higher energies and, in concert with the loss processes, provides exponential spectral form as a function of energy.

Plain Language Summary The dynamics of the highly energized populations of charged particles encircling Earth known as the radiation belts continue to challenge understanding. In this research the global effect of low frequency electromagnetic (Alfvénic) fluctuations pervading the outer "belt" of electrons is evaluated—an endeavor not previously attempted. Statistical models based on measurements and theory that quantify the rates at which these fluctuations scatter outer belt electrons are used to study the evolution of the distribution of these particles through near Earth space. It is found that the action of these fluctuations drives depletions of energetic electron populations via losses to Earth's atmosphere, the outer reaches of Earth's geomagnetic field and to interplanetary space. These losses are shown to occur on time-scales comparable to those required for the observed depletion or "drop-out" of outer belt electron populations during the main phase of the strongest space weather events known as geomagnetic storms. The modeled statistical distribution of the evolving electron populations in velocity and energy appears also to be consistent with that measured from spacecraft flying through the outer belt during these disturbed intervals. The conclusion is that these Alfvénic fluctuations are likely an important, yet unrecognized, driver of outer radiation belt dynamics.

1. Introduction

Observations through Earth's outer radiation belt suggest that there is a driver of radiation belt dynamics that is not included in existing physical models. This omission is implicit in the global distribution of radiation belt electron losses to the atmosphere measured from balloons and by spacecraft in low Earth orbit (e.g., Blum et al., 2015; Comess et al., 2013; Millan et al., 2002; Shekhar et al., 2017; Smith et al., 2016) and that of those wave modes classically identified as drivers of this loss (Breneman & Blum, 2018; Jaynes & Usanova, 2019; Smith et al., 2016; Thorne, 2010). In the equatorial plane these modes have a distribution represented qualitatively by Thorne (2010) and reproduced here as the blue-mauve colored segments shown in Figure 1a. It is a curious fact that the observations of relativistic electron losses to the atmosphere cited above show a distribution peaked pre-midnight where the "canonical" modes represented here by the colored shading are largely absent. While the mechanisms for atmospheric loss involve a complex combination of scattering and transport in Earth's inhomogeneous magnetic field (Millan & Thorne, 2007), this apparent discrepancy nonetheless represents a challenge for understanding losses to the atmosphere based on interactions in the canonical wave modes and their distributions identified in Figure 1a.

The gray scale in Figure 1a shows the qualitative distribution of broad spectrum Alfvénic fluctuations in the equatorial plane. This distribution is based on statistical studies across the magnetopause and through the inner magnetosphere and plasma sheet (Chaston et al., 2012, 2015; Yao et al., 2011). These turbulent fields comprise a spectrum of electromagnetic fluctuations extending across scales from those of classical shear Alfvén modes

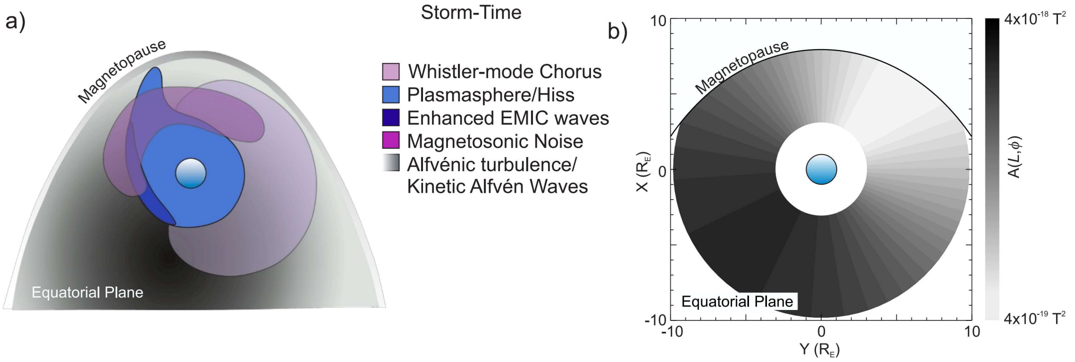

Figure 1. (a) Qualitative equatorial distribution of plasma wave modes active in the modulation of radiation belt electrons based on Thorne (2010) with the addition of Alfvénic turbulence/kinetic Alfvén waves. (b) Distribution of spectral energy density of Alfvénic turbulence within $L = 10$ as used in the transport simulation.

through to dispersive scales that in the equatorial plane correspond to kinetic Alfvén waves (Chaston et al., 2014, 2015; Malaspina et al., 2015; Moya et al., 2015). These broadband fluctuations have scales perpendicular to the geomagnetic field spanning thermal ion gyro-radii and encompassing the full range of outer radiation belt electron gyro-radii. They are highly extended along the geomagnetic field with parallel scales in the inner magnetosphere that are a significant fraction of a field-line length between ionospheres. These wavefields often show phase characteristics consistent with counter-propagation and kinetic Alfven eigenmodes of the field-line sometimes referred to as kinetic field-line resonances (Chaston et al., 2014; Damiano et al., 2018; Hull et al., 2023). They are a nearly permanent feature of the storm time inner magnetosphere outside the plasmapause and unlike the spatial distribution of those modes classically identified as drivers of radiation belts losses in Figure 1a, have a distribution in L-shell and local time in the inner magnetosphere coincident with that of the measured losses of relativistic electrons in those works cited above (Chaston et al., 2015). This coincidence motivates the numerical study pursued in this letter to examine the transport of outer radiation belt electrons through L-shell, equatorial pitch-angle (α) and momentum space (p) in the observed Alfvénic turbulence.

2. Transport Modeling

To provide a means to evaluate the effect of the observed broad-spectrum Alfvénic wave fields on the outer belt a Monte Carlo approach is implemented (Retterer et al., 1983) using bounce averaged transport coefficients derived from explicit tracing of outer belt electrons in observationally defined Alfvénic field variations (Chaston, 2023). This approach reduces the numerical burden of explicitly solving the equation of motion on sub-cyclotron timescales to a series of perturbations or shifts in L-shell (ΔL), equatorial pitch-angle ($\Delta\alpha$) and scalar momentum (Δp) with each shift separated in time by the bounce period (τ_b). The size of each shift is derived from the statistical distribution of shifts defined by the bounce averaged transport coefficients. For a sufficiently large number of electrons perturbed in this manner the evolution of the electron distribution (f) is determined by the probability distribution $P_{\tau_b}(\Delta L,\, \Delta\,\alpha,\, \Delta\, p; L,\alpha,p)$ of the perturbations and described by,

$$f(L,\alpha,p,t+\tau_b) = \int f(L-\Delta L,\alpha-\Delta\alpha,p-\Delta p,t)\, P_{\tau_b}(\Delta L,\Delta\alpha,\Delta p; L,\alpha,p)\, d\Delta L\, d\Delta\alpha\, d\Delta p \tag{1}$$

To simplify the evaluation of P_{τ_b} it is noted that the diffusion in L and α is primarily due to the action of the wave magnetic field (Chaston, 2023; Chaston, Bonnell, Halford, et al., 2018; Chaston, Bonnell, Wygant, et al., 2018) and necessarily occurs at constant energy (E_n) with no change in p. On the other hand, the covariance of ΔL and $\Delta\alpha$ is defined by the relationship,

$$\Delta\alpha_L \approx \tan^{-1}\left[\frac{\beta-\tan\alpha}{1+\beta\tan\alpha}\right] \text{ where } \beta = \sqrt{\frac{L^3\sin^2\alpha}{(L+\Delta L)^3 - L^3\sin^2\alpha}} \tag{2}$$

after Chaston, Bonnell, Wygant, et al. (2018; Equation 6), noting that $\Delta L > L(\sin^{2/3}\alpha - 1)$ and as $(L + \Delta L)^3 - L^3 \sin^2\alpha \to 0$ then $\Delta\alpha \to \frac{\pi}{2} - \alpha$. Under these circumstances P_{τ_b} may be reduced to,

$$P_{\tau_b}(\Delta L, \Delta\alpha, \Delta p; L, \alpha, p) \approx P_{\tau_b}(\Delta L; L)\, P_{\tau_b}(\Delta\alpha; \alpha)\, P_{\tau_b}(\Delta p; p) \tag{3}$$

where $P_{\tau_b}(\Delta\vartheta; \vartheta)$ is related to the bounce averaged transport coefficients $(D_{\vartheta\vartheta})$ via its 2nd order moment as $\langle(\Delta\vartheta)^2\rangle = 2D_{\vartheta\vartheta}\tau_b$ with first order moments $\langle\Delta L\rangle = 0$, $\langle\Delta\alpha\rangle = \Delta\alpha_L$ and $\langle\Delta p\rangle = 0$. Provided $\tau_b \ll 1/D_{\vartheta\vartheta}$, the statistical displacement of an electron over N bounces is then,

$$\Delta\vartheta(N\tau_b) = \sum_{j=0}^{N} \Delta\vartheta_j \tag{4}$$

where $\Delta\vartheta$ is ΔL, $\Delta\alpha$ or Δp and distributed according to $P_{\tau_b}(\Delta\vartheta; \vartheta)$. It was demonstrated in Chaston (2023) that over the range of outer radiation belt energies $P_{\tau_b}(\Delta\vartheta)$ has Gaussian form. Consequently, the evolution of the particle distributions in these quantities can be followed by random selection of $\Delta\vartheta_j$ from a normal distribution with standard deviation $\sqrt{2D_{\vartheta\vartheta}\tau_b}$ applied to a large number of particles representative of distributions in the outer radiation belt.

In addition to diffusive transport, curvature-gradient drift is included in a bounce averaged manner to provide an azimuthal displacement given as $\Delta\phi = 2\pi\tau_b/\tau_D$ where τ_D is the drift period and ϕ is measured in the direction of electron drift or anticlockwise from midnight if looking downward from above the north pole. In principle, drifts in an imposed convection electric field within a distorted dipole geomagnetic field could also be considered, however, to isolate the effect of the wave-particle interactions this is not implemented here.

The requisite $D_{\vartheta\vartheta}$ are based on statistics provided by the full solution of electron trajectories in a dipolar field model that replicates the 3-D structure and spectrum of the observed EM turbulence. This model comprises those wave-scales relevant for examining interactions with electron orbits over an energy range from 50 keV to 5 MeV (Chaston, 2023). The coefficients are evaluated for log-normal averaged spectral statistics compiled along all Van Allen Probes traversals through Alfvénic turbulence over the years 2013–2015. The coefficients are derived for wave solutions at $L = 5.7$ and extrapolated across L and through longitude using the statistical variation in observed spectral energy densities reported in Chaston et al. (2015; Figure 5) and approximate scaling factors given by expressions for the local time rate of change in L,α and p from Chaston (2023). The scaling factors are $\left(\frac{L}{L_{5.7}}\right)^7$, $\left(\frac{L}{L_{5.7}}\right)^2$ and $\left(\frac{L}{L_{5.7}}\right)^2$, respectively as derived in Supporting Information S1. The observed magnetic wave spectrum has form $\varepsilon_s = A(L,\phi)s^{-\zeta}$ in units T^2/ds where $s = k_\perp\rho_i$, $k_\perp$ is the perpendicular wavenumber, ρ_i the thermal ion gyro-radius and $\zeta = 2$. Since ζ is fixed then $D_{\vartheta\vartheta} \propto A$ for fixed L and ϕ. Observations show no clear secular variation in A with L from $L = 3$ to 6, however spectral energy densities peak pre-midnight and generally decrease toward the dayside (Chaston et al., 2015). This morphology is parameterized as,

$$A(L, \phi) = A_0\kappa e^{-\left(\cos\left[(\phi-\phi_o-\pi)/2\right]/\phi_w\right)^2} \tag{5}$$

where $A_0 = 4 \times 10^{-18}\ T^2$, $\kappa = 2$, $\phi_o = 7\pi/4$ is the location in longitude (or local time) of peak spectral energy density corresponding to a local time of 22:30, with $\phi_w = \pi/4$ defining the wave distribution width in longitude. The value used for A_0 replicates the observed magnetic spectrum averaged across all Van Allen Probes measurements formulated as $\varepsilon_s = A_0 s^{-\zeta}$ (Chaston, 2023; Figure 1). The standard deviation in the logarithm of the observed distribution in $A_{0'}$ and hence $D_{\vartheta\vartheta'}$ is ~1 (Chaston et al., 2015). Variations within one standard deviation from the averages used here will therefore change the timescales described in what follows by up to a factor of ~3. $\kappa = 2$ in Equation 5 provides peak spectral energy densities at $\phi_o = 7\pi/4$ that are twice the average. This parameterization, while not capturing the fine-scale structure of the spatial distributions in these observables, is qualitatively consistent with that observed and sufficient for the purpose of this letter.

The spatial distribution of A provided by Equation 5 is shown in Figure 1b. The inner boundary here corresponds to the inner-most edge of the observed region of Alfvénic turbulence and nominally the plasmapause. The location of the magnetopause is provided by the model of Shue et al. (1997) with a stand-off distance of 8 Re at the subsolar point and a tail flaring parameter of 0.5 as might be expected during active conditions. An outer boundary for the region considered is placed at $L = 10$. Particles traversing these boundaries are considered “lost.”

To facilitate rapid estimation of the transport coefficients at specific α and E_n we fit the logarithm of the coefficients reported in Chaston (2023) as a function of pitch-angle and energy with a 5th order polynomial of form,

$$\log D_{\vartheta\vartheta} = \sum_{i,j} C_{i,j}\alpha^i \log(E_n)^j \tag{6}$$

which provides an analytical expression for $D_{\vartheta\vartheta}(\alpha, E_n)$ where $C_{i,j}$ are the polynomial coefficients. The coefficients are provided in Supporting Information S1 section. These fits match those values reported in Chaston (2023) to within 20% in the interior of the energy-pitch-angle grid and at worst a factor approaching e at the very largest energy and smallest pitch-angles in D_{pp/p^2} where the value of D_{pp/p^2} is so small that it is not significant in the dynamics.

3. Electron Distributions in Alfvénic Turbulence

To represent a quiescent outer radiation belt an initial distribution composed of 2×10^5 electrons having “pancake” form in pitch-angle is considered with phase space density outside the loss cones varying as $e^{-\cos^2\alpha}$ and $E_n{}^{-\eta}$ over an energy range from 50 keV to 5 MeV. This selection is motivated by studies indicating that pancake and/or flattop distributions are the most commonly observed forms in the outer belt (Killey et al., 2025). These electrons are distributed uniformly in longitude (or ϕ) and relative to the peak phase space density (L_0) as $f \propto (L_0 - L)^{-\chi_-}$ and $f \propto (L - L_0)^{-\chi_+}$ for $L < L_0$ and $L > L_0$, respectively. In the simulation performed $\eta = 2$, $\chi_- = 0.5$, $\chi_+ = 1.0$, and $L_0 = 5.0$ and only electrons on closed drift paths through the region shown in Figure 1b are included. To isolate the effect of the wavefields no “new” electrons are injected into the volume during the simulation and those electrons exiting the range $E_n = 0.025$–10 MeV are discarded.

Figures 2a–2d show the initial distribution at $t = 0$ and subsequent snapshots viewed looking downward onto the equatorial plane as the distribution evolves. The same results integrated in ϕ are shown in Figure 2e. The efficacy of the observed wave spectrum in driving radial transport becomes apparent within a single drift orbit. Figure 2b shows fluxes extending outward to $L = 10$ on trajectories passing through the magnetopause. Electrons are also transported to the inner boundary leading to a spreading of the distribution across L-shells as represented in Figure 2e. As shown in Figures 2c–2e the continued operation of this process leads to a shift of the distribution peak to inside $L = 4$ and an order of magnitude decrease in the total electron content by $t = 16{,}000$ s. This depletion is primarily due to losses through the boundaries and to the atmosphere as shall be discussed momentarily.

The dependency of the transport relative to the classical 1st (μ) and modified 2nd (K) invariants is captured in the remaining panels of Figure 2 with each row providing snapshots at constant μ and K. Specifically, these panels demonstrate the increasing efficacy of the scattering/transport process with increasing μ for electrons that mirror progressively closer to the equator. Here the sequence shown in Figures 2f–2i document an almost complete loss of electrons at $\mu = 500$ MeV/Gauss and $K = 0.02\text{Gauss}^{1/2}R_E$ after 1800s. These values correspond to electrons with $E_n = 500$ keV and $\alpha = 79°$ at $L = 6$ and $E_n = 1{,}200$ keV and $\alpha = 80°$ at $L = 4$. The evacuation of the energetic population becomes even more rapid in the subsequent rows of this figure, showing order magnitude decreases and almost complete depletions at larger values of μ within the drift period of an MeV electron at L_0.

Figure 3 shows example orbits and statistics for the three mechanisms of loss operating within the volume. The curves in Figures 3a–3c trace the location of individual electrons with $E_n = 1$ MeV and $\alpha_o = 45°$ every 4th bounce after the beginning of the simulation. The erratic disturbance of the nominally circular drift orbits in the dipolar background field due to the action of the wavefields is readily apparent and leads to loss at the magnetopause, through the inner boundary and to the atmosphere, respectively. The statistics of where these losses occur is captured in Figures 3d–3f. Losses through the outer boundary occur primarily through the dayside magnetopause and pre-midnight corresponding to the location of the greatest spectral energy density. Losses through the inner boundary are also peaked pre-midnight but more evenly distributed in local time. Losses to the atmosphere are distributed in local time in a manner roughly proportional to the distribution of spectral energy density but are largest at lower L-shell. Of those electrons that remain in the energy range $E_n = 0.025$–10 MeV over 16,000 s, loss

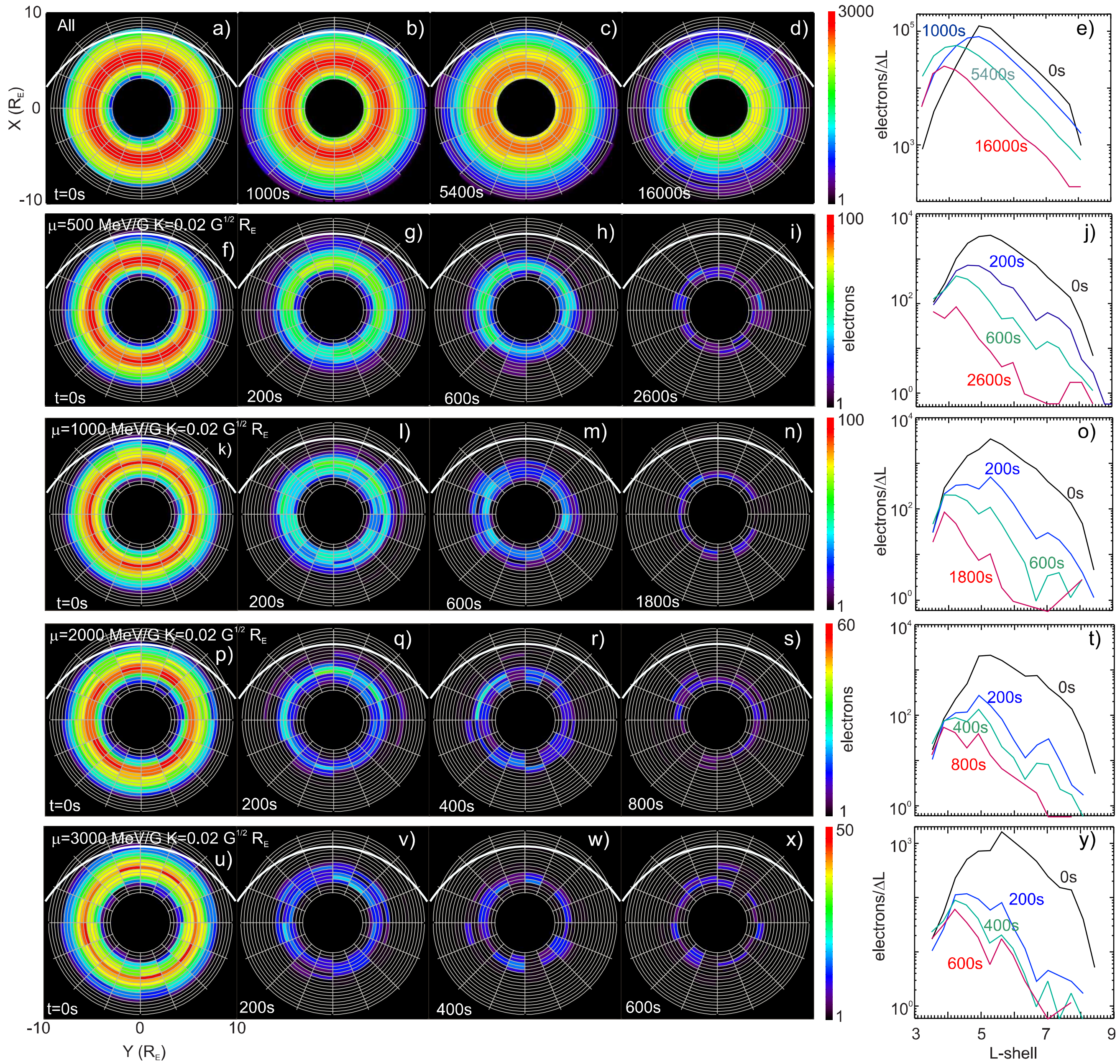

Figure 2. (a–e) Total electron content snapshots of the outer belt in *L*-shell and longitude (local time) at times indicated and (e) integrated over longitude. Noon is at the top in each frame, dawn to the right, and the white line is the magnetopause. Subsequent rows (f–y) have the same format but at fixed values of first (μ) and second (K) adiabatic invariant as indicated on the first panel of each row (note that the time of each snapshot varies between rows).

to the magnetopause and inner plasma sheet accounts for ~40% of the total, losses through the inner boundary comprise ~30%, while losses to the atmosphere correspond to ~3%. The remaining electrons in the radiation belt after this time are nearly entirely at energies below 500 keV.

The spectrum of these losses is shown in Figures 3g–3i. Here the black curve shows the initial omni-directional spectrum in phase space density while the red curve is the spectrum of losses accumulated over 16,000 s. All three red loss curves have "break-points" in energy (E_{nb}) above which the spectrum follows the spectral-form of the source population. From Figure 3g losses due to outward radial transport become significant above $E_{\mathrm{nb}} \sim 100$ keV accounting for a nearly constant fraction of phase space density above this energy. In comparison losses through the inner boundary become most significant above $E_{\mathrm{nb}} \sim 500$ keV, and in this energy range are the dominant

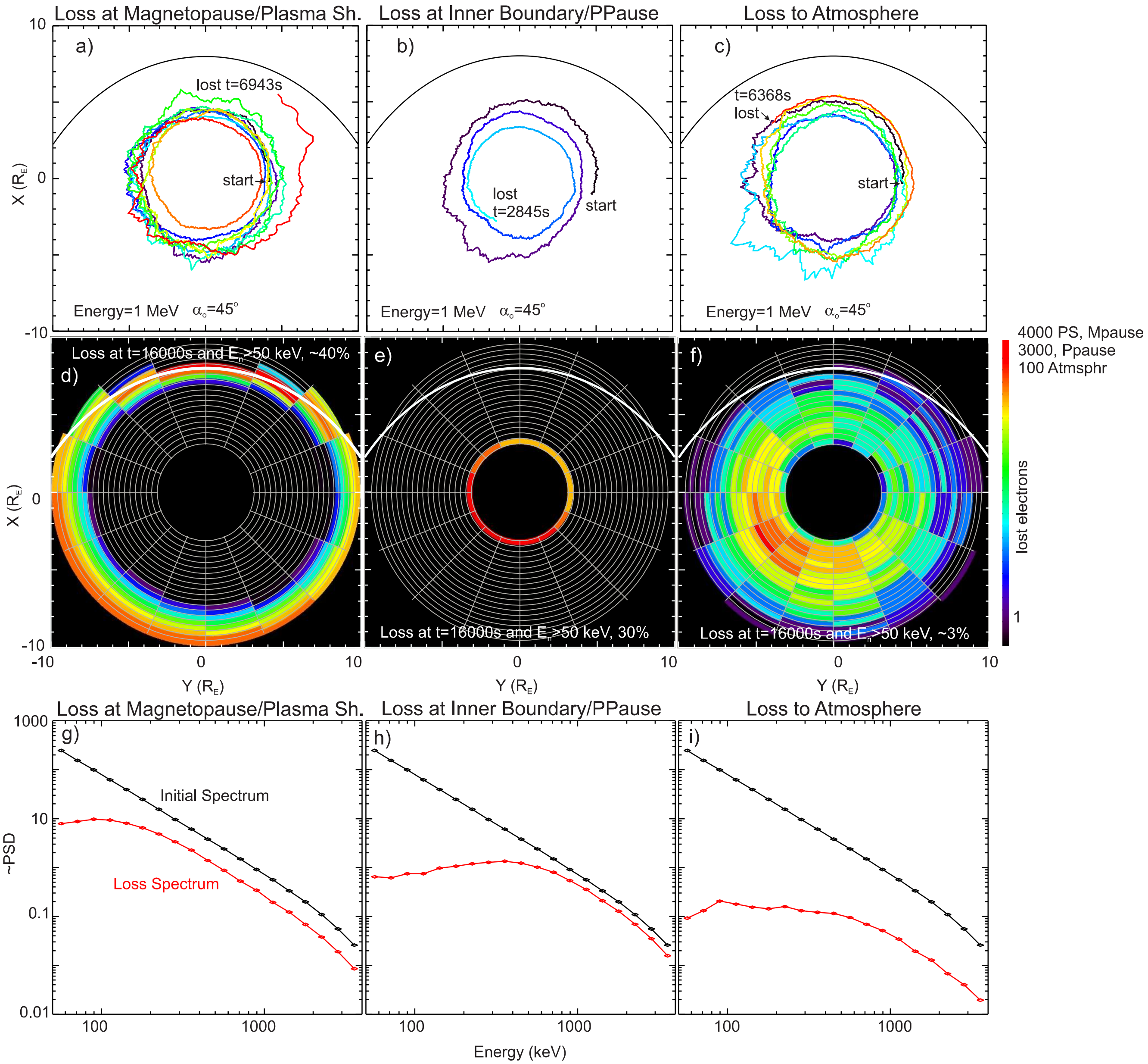

Figure 3. (a–c) Example electron orbits in the equatorial plane starting at similar dawn-side locations with $E_n = 1$ MeV and $\alpha = 45°$ and lost through the magnetopause, plasmapause, and atmosphere, respectively. Line color represents time elapsed. (d–f) Statistics of loss location as indicated. (g–i) Initial energy spectrum in phase space density (black) and spectrum of accumulated losses (red) after 16,000 s.

means of electron loss from the simulation volume. Loss to the atmosphere is a relatively less important mechanism for radiation belt depletion in this model and accounts for less than 10% of phase space density above $E_{\text{nb}} \sim 1$ MeV and a substantially smaller fraction at lower energies. Albeit, in absolute terms the phase space density of losses to the atmosphere slowly increases with decreasing energy below ~1 MeV with the increasing phase space density of the source population. It is also worth noting that the relative contribution of the atmospheric loss process increases with decreasing α (or as $\alpha \rightarrow 180°$).

To provide a representation of what this process looks like in observations, Figure 4 shows snapshots and time-series of the evolving electron energy and pitch-angle spectra. These are integrated over the width of the volume in L-shell and longitude and are representative of what may be observed close to the peak of the distribution. It is, however, noted that there are secondary variations within these coordinates that for brevity will not be considered here. Figures 4a–4d show spectra in phase space density at a number of pitch-angles outside the loss cone. In

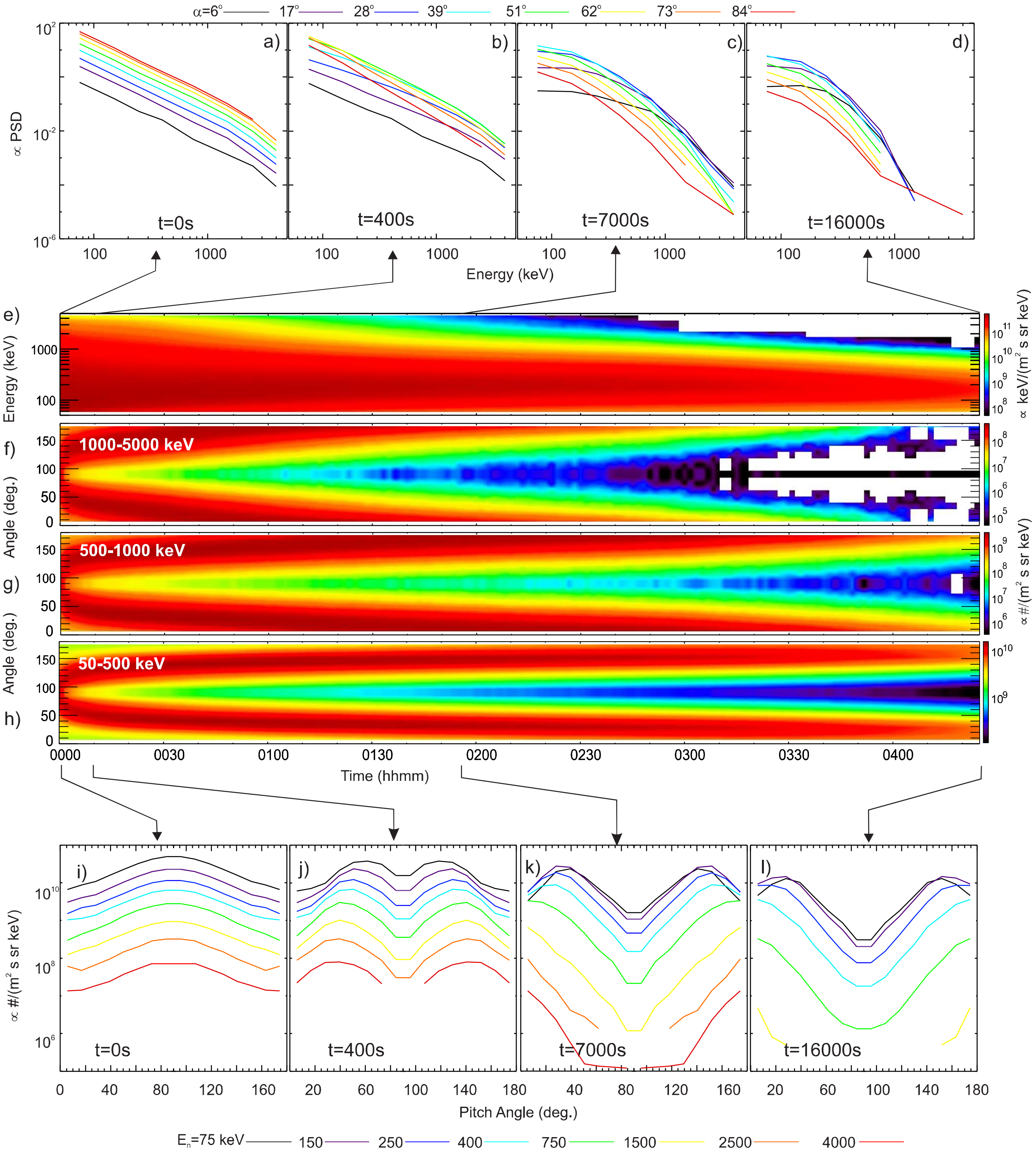

Figure 4. (a–d) Energy spectrum in phase space density for a range of selected equatorial pitch angles (α) and times as indicated. (e) Continuous energy spectra in differential energy flux as a function of time. (f–h) Continuous equatorial pitch-angle spectra in differential flux as a function of time for the energy ranges indicated. (i–l) Equatorial pitch-angle spectra in differential flux for selected energies and times as indicated.

Figure 4a the phase space density peaks at $\alpha = 90°$ with power-law form representing respectively the "pancake" distribution in α and the energy dependency of the unperturbed radiation belt population. After this time there is a progressive decrease in phase space density at large pitch-angle and an evolution from power-law to exponential form. This evolution is a consequence of the depletion of the most energetic electrons in addition to energy changes occurring primarily below 1 MeV through interaction with the wave electric field (Chaston, 2023). This interaction while driving net energization on the negative gradient of phase space density with energy, delivers a loss of energy for a subset of electrons some of which fall below the 25 keV lower limit considered. Eventually even the most field-aligned electrons are depleted at high energy so that after several drift orbits the initial power law has decayed to exponential form across all pitch-angles. The evolution of the omnidirectional spectrum in this manner is captured as a time-energy plot in differential energy flux in Figure 4e. This figure reveals the effective total depletion of the model outer radiation belt above ∼1 MeV after 4 hr of immersion in the empirically derived wave model.

This evolution as a function of pitch-angle is represented in Figures 4f–4h that characterize the corresponding time/pitch-angle spectra in differential flux. Here the formation of “butterfly” distributions peaked at intermediate angles is immediately apparent in each of the energy ranges shown. A progressive transition to more field-aligned form proceeds before total depletion at the higher energies occurs. The finer details of this sequence are captured in Figures 4i–4l. These show transport through pitch-angle associated with local scattering in the wavefields that preferentially operates on higher energy electrons and “digs” a hole in the flux of the evolving distributions that deepens and expands across pitch-angles from $\alpha = 90°$ as a function of time. Eventually, complete loss from the simulation volume is manifested through the progressive decrease in flux across all pitch-angles. The depletion of electron flux at large pitch-angle corresponds to respectively positive and negative gradients in $D_{\alpha\alpha}$ for $\alpha < 90°$ and $\alpha > 90°$ that drive electrons outward from $\alpha = 90°$ in a manner analogous to the operation of the ponderomotive force. The most extreme example of this is captured by the red curve in these figures corresponding to electrons at $E_n \approx 4$ MeV. This curve retains similar flux levels as pitch-angle scattering forms “butterfly” distributions in the transition from Figures 4i and 4j while losses eventually deplete this flux across all pitch-angles in the sequence captured in Figures 4j–4l.

4. Discussion and Conclusion

These simulation results demonstrate the global effect of broad spectrum Alfvénic fluctuations observed through the upper ULF and lower ELF ranges on Earth's outer radiation belt. This research is most pertinent to the main phase of geomagnetic storms when an intensified spectrum of these fluctuations is observed almost continuously outside the nightside plasmapause. The simulation shows that the action of broad-spectrum Alfvén waves drives radial transport and loss through the magnetopause, into the plasma sheet and through the inner edge of the wave region representing the plasmapause. Simultaneously, pitch-angle scattering in these waves drives losses to the atmosphere with a distribution in *L*-shell and local-time that replicates that observed by statistical measurements of relativistic electron precipitation cited in the Introduction. For observed average spectral energy densities these loss processes drive nearly complete depletion of electron populations above 1 MeV on time scales of the order of a few hours and over an interval less than the orbital period of spacecraft traversing the outer belt. Consequently, this mechanism may account for “drop-out” events where the outer belt is observed to effectively disappear between consecutive satellite passes during the main phase of geomagnetic storms (Baker et al., 2016; Turner et al., 2012).

The efficacy of these broad spectrum Alfvénic variations in driving radiation belt modification is a consequence of perpendicular wave scales that encompass the range of radiation belt electron gyro-radii and the correspondence of azimuthal particle drifts over a bounce period with the expected range of azimuthal wave phase velocities on these scales (drift-bounce resonance). The former causes local scattering while the latter leads to radial transport. The process operates via multiple stochastic interactions with the broad spectrum fluctuations over a coherency time, inversely related to the resonant bandwidth that defines the “interaction” amplitude from the observed spectrum (Chaston et al., 2017; Chaston, Bonnell, Wygant, et al., 2018). Numerical simulations (Chaston et al., 2023) show some evidence for extended coherent interactions introducing the possibility of particle trapping (e.g., Li et al., 2024), however these constitute a small fraction of the statistics on which the transport coefficients are based. The electron transport and scattering quantified by these coefficients does not occur in established models for MHD ULF wave transport (Elkington, 2006) because the wavenumbers considered in such models are too small. A description of the wave-particle interactions and wave properties at the core of the dynamics represented by the coefficients can be found in Chaston (2023) and references therein.

There are at least three idiosyncratic aspects of Alfvénic driven transport through pitch-angle and across L-shell in the outer radiation belt. First, because displacements in the radial direction occur primarily through the action of the perturbed magnetic field, the transport across L-shells necessarily proceeds at constant energy. Consequently, the usual connection between radial transport and energization conserving the invariants is broken. Second, scattering in these fluctuations operates in a manner analogous to a ponderomotive force in pitch-angle with transport coefficients peaked at $\alpha = 90°$ driving depletions that expand outward from this pitch-angle on gradients of $D_{\alpha\alpha}$ in α. This process leads to the formation of "butterfly" distributions and with continued action drives transport toward more field-aligned α and eventual loss to the atmosphere. Third the energization and depletion of respectively sub-relativistic and relativistic electrons lead to a flattening of the spectrum at lower energies and a steepening at higher energies to provide exponential spectral forms as a function of energy.

In closing, while these results demonstrate that the action of Alfvénic turbulence should be included in advancing understanding of radiation belt dynamics, a consideration of more realistic evolving field geometries is required to provide quantitative assessment of the role of these turbulent fields through any individual storm and to robustly assess their efficacy relative to the other modes of wave driven transport. This represents a challenge for existing numerical models because the large scale of these turbulent fluctuations along the geomagnetic field, and their small scale in the direction across the geomagnetic field, requires simultaneous resolution of both the global scale evolving field geometry and kinetic scale variations in the perpendicular plane. Such models for Earth's magnetosphere do not currently exist.

Data Availability Statement

All analyses were performed, and plots generated, using the Interactive Data Language (IDL) software available for purchase at nv5geospatialsoftware.com. The full set of data files generated by the transport simulations performed in this research and used in the production of figures in this report are available at Chaston (2025, https://doi.org/10.5281/zenodo.14727333) in the form of compressed (zip) IDL save files that can be extracted after download using the IDL "Restore" command (https://www.nv5geospatialsoftware.com/docs/restore.html). A PDF file describing the quantities in these data files is also provided at this site. The eigenmode solutions and plasma model defining the turbulent wavefields as described in Chaston (2023), along with files containing the transport coefficients extracted from the particle tracing used in this manuscript are available at https://doi.org/10.6084/m9.figshare.22672933.v1 in the form of delimited text files with license https://creativecommons.org/licenses/by/4.0/. A PDF file describing the file contents and format is also provided at this site.

Acknowledgments
The author thanks the Van Allen Probes team for the in situ measurements which motivated this study and defined the field model. Conversations with Dr. Krushna Chandra Barik on observations of energetic electron distributions in Alfvénic turbulence are acknowledged. This research was supported by NSF Grants 2041971 and 2411605.

References

Baker, D. N., Jaynes, A. N., Kanekal, S. G., Foster, J. C., Erickson, P. J., Fennell, J. F., et al. (2016). Highly relativistic radiation belt electron acceleration, transport, and loss: Large solar storm events of March and June 2015. *Journal of Geophysical Research: Space Physics*, *121*(7), 6647–6660. https://doi.org/10.1002/2016JA022502

Blum, L., Li, X., & Denton, M. (2015). Rapid MeV electron precipitation as observed by SAMPEX/HILT during high-speed stream-driven storms. *Journal of Geophysical Research: Space Physics*, *120*(5), 3783–3794. https://doi.org/10.1002/2014JA020633

Breneman, A., & Blum, L. (2018). Observations of radiation belt losses due to cyclotron wave-particle interactions. In A. Jaynes & M. Usanova (Eds.), *The dynamic loss of Earth's radiation belts: From loss in the magnetosphere to particle precipitation in the atmosphere* (1st ed., p. 400). Elsevier.

Chaston, C. C. (2025). Data files for radiation belt transport and scattering simulation [Dataset]. *Zenodo*. https://doi.org/10.5281/zenodo.14727333

Chaston, C. C. (2023). Electron scattering, transport and energization by Alfvénic turbulence in Earth's outer radiation belt [Dataset]. *Geophysical Research Letters*, *50*(13), e2023GL104243. https://doi.org/10.1029/2023GL104243

Chaston, C. C., Bonnell, J. W., Clausen, L., & Angelopoulos, V. (2012). Correction to "Energy transport by kinetic-scale electromagnetic waves in fast plasma sheet flows". *Journal of Geophysical Research*, *117*(A12), A12205. https://doi.org/10.1029/2012JA018476

Chaston, C. C., Bonnell, J. W., Halford, A. J., Reeves, G. D., Baker, D. N., Kletzing, C. A., & Wygant, J. R. (2018). Pitch angle scattering and loss of radiation belt electrons in broadband electromagnetic waves. *Geophysical Research Letters*, *45*(18), 9344–9352. https://doi.org/10.1029/2018GL079527

Chaston, C. C., Bonnell, J. W., Kletzing, C. A., Hospodarsky, G. B., Wygant, J. R., & Smith, C. W. (2015). Broadband low-frequency electromagnetic waves in the inner magnetosphere. *Journal of Geophysical Research: Space Physics*, *120*(10), 8603–8615. https://doi.org/10.1002/2015JA021690

Chaston, C. C., Bonnell, J. W., Wygant, J. R., Mozer, F., Bale, S. D., Kersten, K., et al. (2014). Observations of kinetic scale field line resonances. *Geophysical Research Letters*, *41*(2), 209–215. https://doi.org/10.1002/2013GL058507

Chaston, C. C., Bonnell, J. W., Wygant, J. R., Reeves, G. D., Baker, D. N., & Melrose, D. B. (2018). Radiation belt "dropouts" and drift-bounce resonances in broadband electromagnetic waves. *Geophysical Research Letters*, *45*(5), 2128–2137. https://doi.org/10.1002/2017GL076362

Chaston, C. C., Bonnell, J. W., Wygant, J. R., Reeves, G. D., Baker, D. N., Melrose, D. B., & Cairns, I. H. (2017). Radial transport of radiation belt electrons in kinetic field-line resonances. *Geophysical Research Letters*, *44*(16), 8140–8148. https://doi.org/10.1002/2017GL074587

Comess, M. D., Smith, D. M., Selesnick, R. S., Millan, R. M., & Sample, J. G. (2013). Duskside relativistic electron precipitation as measured by SAMPEX: A statistical survey. *Journal of Geophysical Research: Space Physics*, *118*(8), 5050–5058. https://doi.org/10.1002/jgra.50481

Damiano, P. A., Chaston, C. C., Hull, A. J., & Johnson, J. R. (2018). Electron distributions in kinetic scale field line resonances: A comparison of simulations and observations. *Geophysical Research Letters*, *45*(12), 5826–5835. https://doi.org/10.1029/2018GL077748

Elkington, S. R. (2006). A review of ULF interactions with radiation belt electrons. In K. Takahashi, P. J. Chi, R. E. Deton, & R. L. Lysak (Eds.), *Magnetospheric ULF waves: Synthesis and new directions* (p. 177). American Geophysical Union. https://doi.org/10.1029/169GM12

Hull, A. J., Chaston, C. C., Damiano, P. A., Frey, H. U., & Wing, S. (2023). Multipoint observations of dispersive scale Alfvénic field-line resonances associated with substorm auroral beads. *Journal of Geophysical Research: Space Physics*, *128*(2), e2021JA029823. https://doi.org/10.1029/2021JA029823

Jaynes, A. & Usanova, M. (Eds.) (2019). *The dynamic loss of Earth's radiation belts: From loss in the magnetosphere to particle precipitation in the atmosphere* (1st ed.). Elsevier.

Killey, S., Rae, I. J., Smith, A. W., Bentley, S. N., Watt, C. E. J., Chakraborty, S., et al. (2025). Identifying typical relativistic electron pitch angle distributions: Evolution during geomagnetic storms. *Geophysical Research Letters*, *52*(3), e2024GL112900. https://doi.org/10.1029/2024GL112900

Li, L., Zhou, X.-Z., Omura, Y., Zong, Q.-G., Liu, Y., Rankin, R., et al. (2024). Nonlinear drift-bounce resonance between charged particles and ultralow frequency waves. *Journal of Geophysical Research: Space Physics*, *129*(8), e2024JA032742. https://doi.org/10.1029/2024JA032742

Malaspina, D. M., Claudepierre, S. G., Takahashi, K., Jaynes, A. N., Elkington, S. R., Ergun, R. E., et al. (2015). Kinetic Alfvén waves and particle response associated with a shock-induced, global ULF perturbation of the terrestrial magnetosphere. *Geophysical Research Letters*, *42*(21), 9203–9212. https://doi.org/10.1002/2015GL065935

Millan, R. M., Lin, R. P., Smith, D. M., Lorentzen, K. R., & McCarthy, M. P. (2002). X-ray observations of MeV electron precipitation with a balloon-borne germanium spectrometer. *Geophysical Research Letters*, *29*(24), 2194. https://doi.org/10.1029/2002GL015922

Millan, R. M., & Thorne, R. M. (2007). Review of radiation belt relativistic electron loss. *Journal of Atmospheric and Solar-Terrestrial Physics*, *69*(3), 362–377. https://doi.org/10.1016/j.jastp.2006.06.019

Moya, P. S., Pinto, V. A., Viñas, A. F., Sibeck, D. G., Kurth, W. S., Hospodarsky, G. B., & Wygant, J. R. (2015). Weak kinetic Alfvén waves turbulence during the November 14th 2012 geomagnetic storm: Van Allen Probes observations. *Journal of Geophysical Research: Space Physics*, *120*, 5504–5523. https://doi.org/10.1002/2014JA020281

Retterer, J. M., Chang, T., & Jasperse, J. R. (1983). Ion acceleration in the supra-auroral region: A Monte Carlo model. *Geophysical Research Letters*, *10*(7), 583–586. https://doi.org/10.1029/GL010i007p00583

Shekhar, S., Millan, R., & Smith, D. (2017). A statistical study of the spatial extent of relativistic electron precipitation with polar orbiting environmental satellites. *Journal of Geophysical Research: Space Physics*, *122*(11), 11274–11284. https://doi.org/10.1002/2017JA024716

Shue, J.-H., Chao, J. K., Fu, H. C., Russell, C. T., Song, P., Khurana, K. K., & Singer, H. J. (1997). A new functional form to study the solar wind control of the magnetopause size and shape. *Journal of Geophysical Research*, *102*(A5), 9497–9511. https://doi.org/10.1029/97JA00196

Smith, D. M., Casavant, E. P., Comess, M. D., Liang, X., Bowers, G. S., Selesnick, R. S., et al. (2016). The causes of the hardest electron precipitation events seen with SAMPEX. *Journal of Geophysical Research: Space Physics*, *121*(9), 8600–8613. https://doi.org/10.1002/2016JA022346

Thorne, R. M. (2010). Radiation belt dynamics: The importance of wave-particle interactions. *Geophysical Research Letters*, *37*(22), L22107. https://doi.org/10.1029/2010GL044990

Turner, D. L., Shprits, Y., Hartinger, M., & Angelopoulos, V. (2012). Explaining sudden losses of outer radiation belt electrons during geomagnetic storms electrons during geomagnetic storms. *Nature Physics*, *8*(3), 208–212. https://doi.org/10.1038/nphys2185

Yao, Y., Chaston, C. C., Glassmeier, K.-H., & Angelopoulos, V. (2011). Electromagnetic waves on ion gyro-radii scales across the magnetopause. *Geophysical Research Letters*, *38*(9), L09102. https://doi.org/10.1029/2011GL047328

References From the Supporting Information

Cummings, W. D., O'Sullivan, R. J., & Coleman, P. J., Jr. (1969). Standing Alfvén waves in the magnetosphere. *Journal of Geophysical Research*, *74*(3), 778–793. https://doi.org/10.1029/JA074i003p00778

Dungey, J. (1964). Effects of electromagnetic perturbations on particles trapped in the radiation belts. *Space Science Reviews*, *4*(2), 199–222. https://doi.org/10.1007/bf00173882

Shulz, M., & Lanzerotti, L. J. (1974). *Particle diffusion in the radiation belts, physics and chemistry in space 7*. Springer-Verlag. https://doi.org/10.1007/978-3-642-65675-0